Journal of Glaciology (2017), **63**(241) 888–898 doi: 10.1017/jog.2017.56
© The Author(s) 2017. This is an Open Access article, distributed under the terms of the Creative Commons Attribution licence (http://creativecommons.org/licenses/by/4.0/), which permits unrestricted re-use, distribution, and reproduction in any medium, provided the original work is properly cited.

Sea-ice thickness in the coastal northeastern Chukchi Sea from moored ice-profiling sonar

YASUSHI FUKAMACHI,[1,2,3] DAISUKE SIMIZU,[1,4] KAY I. OHSHIMA,[1,2] HAJO EICKEN,[5] ANDREW R. MAHONEY,[2,3,6] KATSUSHI IWAMOTO,[4,7,8] ERIKA MORIYA,[9,10] SOHEY NIHASHI[11]

[1]*Institute of Low Temperature Science, Hokkaido University, Sapporo, Japan*
[2]*Arctic Research Center, Hokkaido University, Sapporo, Japan*
[3]*Global Station for Arctic Research, Global Institution for Collaborative Research and Education, Hokkaido University, Sapporo, Japan*
[4]*National Institute of Polar Research, Tachikawa, Japan*
[5]*International Arctic Research Center, University of Alaska Fairbanks, Fairbanks, Alaska, USA*
[6]*Geophysical Institute, University of Alaska Fairbanks, Fairbanks, Alaska, USA*
[7]*City of Mombetsu, Mombetsu, Japan*
[8]*Graduate School of Fisheries Sciences, Hokkaido University, Hakodate, Japan*
[9]*Graduate School of Environmental Science, Hokkaido University, Sapporo, Japan*
[10]*Hydro Systems Development, Inc., Tokyo, Japan*
[11]*Department of Mechanical Engineering for Innovation, National Institute of Technology, Tomakomai College, Tomakomai, Japan*
Correspondence: Yasushi Fukamachi <yasuf@lowtem.hokudai.ac.jp>

ABSTRACT. Time series ice-draft data were obtained from moored ice-profiling sonar (IPS), in the coastal northeastern Chukchi Sea during 2009/10. Time series data show seasonal growth of sea-ice draft, occasionally interrupted by coastal polynya. The sea-ice draft distribution indicates a slightly lower abundance of thick, deformed ice compared with the eastern Beaufort Sea. In January, a rapid increase in the abundance of thick ice coincided with a period of minimal drift indicating compaction again the coast and dynamical thickening. The overall mean draft and corresponding derived thickness are 1.27 and 1.38 m, respectively. The evolution of modal ice thickness observed can be explained mostly by thermodynamic growth. The derived ice thicknesses are used to estimate heat losses based on ERA-interim data. Heat losses from the raw, 1 s IPS data are ~50 and 100% greater than those calculated using IPS data averaged over spatial scales of ~20 and 100 km, respectively. This finding demonstrates the importance of subgrid-scale ice-thickness distribution for heat-loss calculation. The heat-loss estimate based on thin ice data derived from AMSR-E data corresponds well with that from the 1 s observed ice-thickness data, validating heat-loss estimates from the AMSR-E thin ice-thickness algorithm.

KEYWORDS: sea ice, sea-ice geophysics, sea-ice growth and decay

1. INTRODUCTION

The coastal Chukchi Sea off northern Alaska is a key region between the Pacific and Canada Basin in the Arctic, since the dominant branch of Pacific Water flows along this coast as the Alaskan Coastal Current (Paquette and Bourke, 1974). In summer and early fall, this current is strong and carries warm, fresh Alaskan Coastal Water (Paquette and Bourke, 1974). In late fall and winter, this current is weak and carries cold, saline Pacific Winter Water (Weingartner and others, 1998), which results from cooling and brine rejection associated with sea-ice production in a series of coastal polynyas in the region (Cavalieri and Martin, 1994). The water mass produced in these polynyas is important in maintaining the Arctic halocline layer that isolates the surface layer from warm Atlantic Water underneath (Melling and Lewis, 1982; Cavalieri and Martin, 1994).

Due to its oceanographic importance and implications for sea ice, this region has been examined in a number of studies through in situ observations, remote sensing and modeling (e.g., Cavalieri and Martin, 1994; Weingartner and others, 1998; Winsor and Björk, 2000; Signorini and Cavalieri, 2002; Winsor and Chapman, 2002; Martin and others, 2004, 2005; Singh and others, 2011; Tamura and Ohshima, 2011; Itoh and others, 2012; Iwamoto and others, 2013, 2014; Ladd and others, 2016). However, in contrast with the adjacent Beaufort Sea (Melling and Riedel, 1995, 1996; Melling and others, 2005; Krishfield and others, 2014), there have been few published studies based on in situ time series measurements of the thickness of pack ice in the Chukchi Sea. We note that extensive work has been carried out on nearby landfast sea ice (e.g., Mahoney and others, 2007, 2014; Druckenmiller and others, 2009). Also, Valenti (2015) carried out a preliminary, engineering-focused analysis of sea-ice thickness using data acquired by the oil and gas industry, which has recently been made available to the public.

In 2009, a mooring equipped with an ice-profiling sonar (IPS) and an acoustic Doppler current profiler (ADCP) was deployed near Point Barrow, Alaska, to measure the thickness and velocity of drifting sea ice and strengthen the existing sea-ice observation network in the region. This paper

https://doi.org/10.1017/jog.2017.56 Published online by Cambridge University Press

presents the first detailed discussion of sea-ice characteristics in the coastal northeastern Chukchi Sea based on such time series data. Taking advantage of the high temporal resolution of the data from the moored instruments, effects of non-uniform ice-thickness distribution on heat loss from the ocean to the atmosphere are also examined. Furthermore, heat losses based on the ice-thickness time series obtained by the IPS are compared with that based on thin ice thicknesses estimated from AMSR-E (Advanced Microwave Scanning Radiometer – Earth Observing System Sensor) data by Iwamoto and others (2013, 2014) to evaluate the validity of the satellite-based estimates.

2. DATA AND METHODS

A mooring was deployed on 7 August 2009 ~23 km off Utqiaġvik (formerly known as Barrow) (71°14.2′N, 157° 39.2′W), where the water depth is 55 m (solid square in Fig. 1). It was recovered on 29 July 2010. The mooring contained an IPS (ASL Environmental Sciences IPS5 420 kHz) at the depth of 35 m, an ADCP (Teledyne RD Instruments WH-Sentinel 300 kHz) at 48 m and a conductivity-temperature recorder (Sea-Bird Electronics SBE37) at 41 m. Note that data collection by the ADCP stopped on 9 June due to battery exhaustion. The IPS sampling intervals were 1 s for range data (distances to ice bottom or ocean surface) and 30 s for pressure and tilt data. The ADCP measured ice velocity using the bottom-tracking mode as well as water-column velocity using the water-tracking mode (Melling and others, 1995). Its sampling interval was 15 min and the bin size for water-column velocity was 2 m. Atmospheric pressure data used to process the IPS data and surface-wind data used to process the ADCP data were measured at Barrow Wiley-Post Airport 32 km away from the mooring location (open square in Fig. 1).

The methods of data processing in this study essentially follow previous work in the Beaufort Sea (Melling and Riedel, 1995, 1996) and the Sea of Okhotsk (Fukamachi and others, 2003, 2006, 2009). Their details are described by ASL Environmental Sciences (2014). Also, general discussions of IPS data processing are found in Melling and others (1995), Strass (1998) and Behrendt and others (2013). The mooring experienced severe tilt during periods of strong currents (Fig. 2e). Any IPS data with combined pitch and roll exceeding 8° (ASL Environmental Sciences, 2014) and ADCP data with pitch or roll exceeding 20° were discarded to improve accuracy of final data. Corrections for sound-speed variations were made by identifying open water above the IPS and reconciling the measured echo travel time with the depth determined from the IPS's pressure sensor. During prolonged periods of high ice concentration, sound speed estimated from the conductivity-temperature recorder was also used. Through this process, the draft of the level ice is typically accurate within ±0.1 m or better. The ice-velocity data were used to convert the draft time series into a pseudo-spatial series. For this purpose, a continuous time series of ice velocity is necessary to estimate the width of the ice-free areas and therefore ice concentration. To estimate ice velocity within data gaps, a multi-linear regression of ice velocity against subsurface water velocity from the intermediate ADCP bin (18–20 m deep) and surface wind measured at Barrow Wiley-Post Airport was performed. The ice-draft data discussed statistically in the following sections are the pseudo-spatial series re-sampled to equal along-track spatial increments of 1 m.

To convert our measurements of ice draft to estimates of ice thickness, we use the concept of the thickness-weighted average density of the ice cover with its snow layer:

$$\rho^* = \frac{\rho_i z_i + \rho_s z_s}{z_i + z_s}, \quad (1)$$

where ρ_i and ρ_s are the densities of ice and snow, respectively, and z_i and z_s are the thickness of ice and snow, also

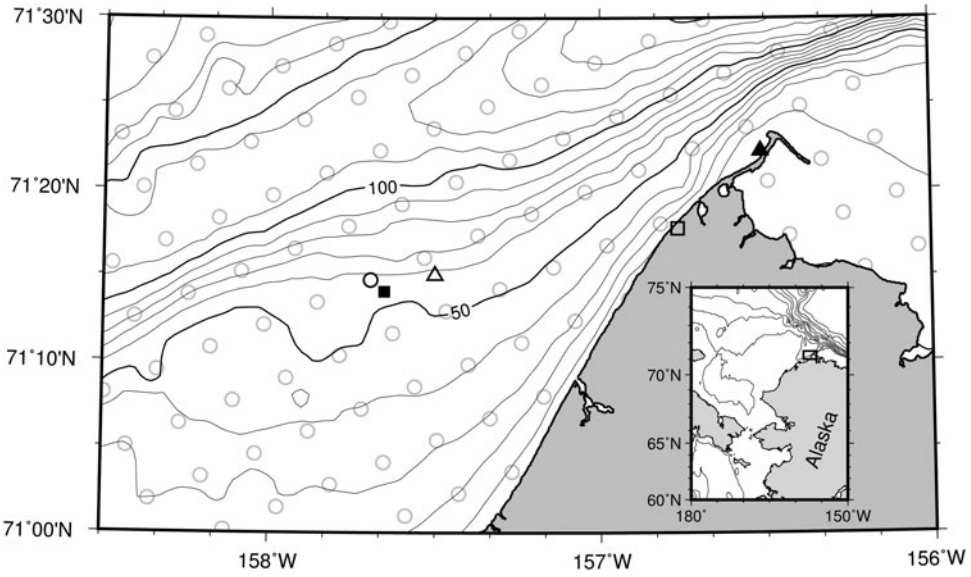

Fig. 1. A bathymetry map of the study region indicating the mooring location (solid square), AMSR-E (gray and black circles) and ERA-Interim grid points (open triangle), Barrow Wiley-Post Airport (open square) and mass-balance station (solid triangle). Note that the AMSR-E grid point closest to the mooring is indicated by a black circle. The inset map shows the surrounding region. The square region around the northern tip of Alaska in the inset map is the region of the enlarged map.

https://doi.org/10.1017/jog.2017.56 Published online by Cambridge University Press

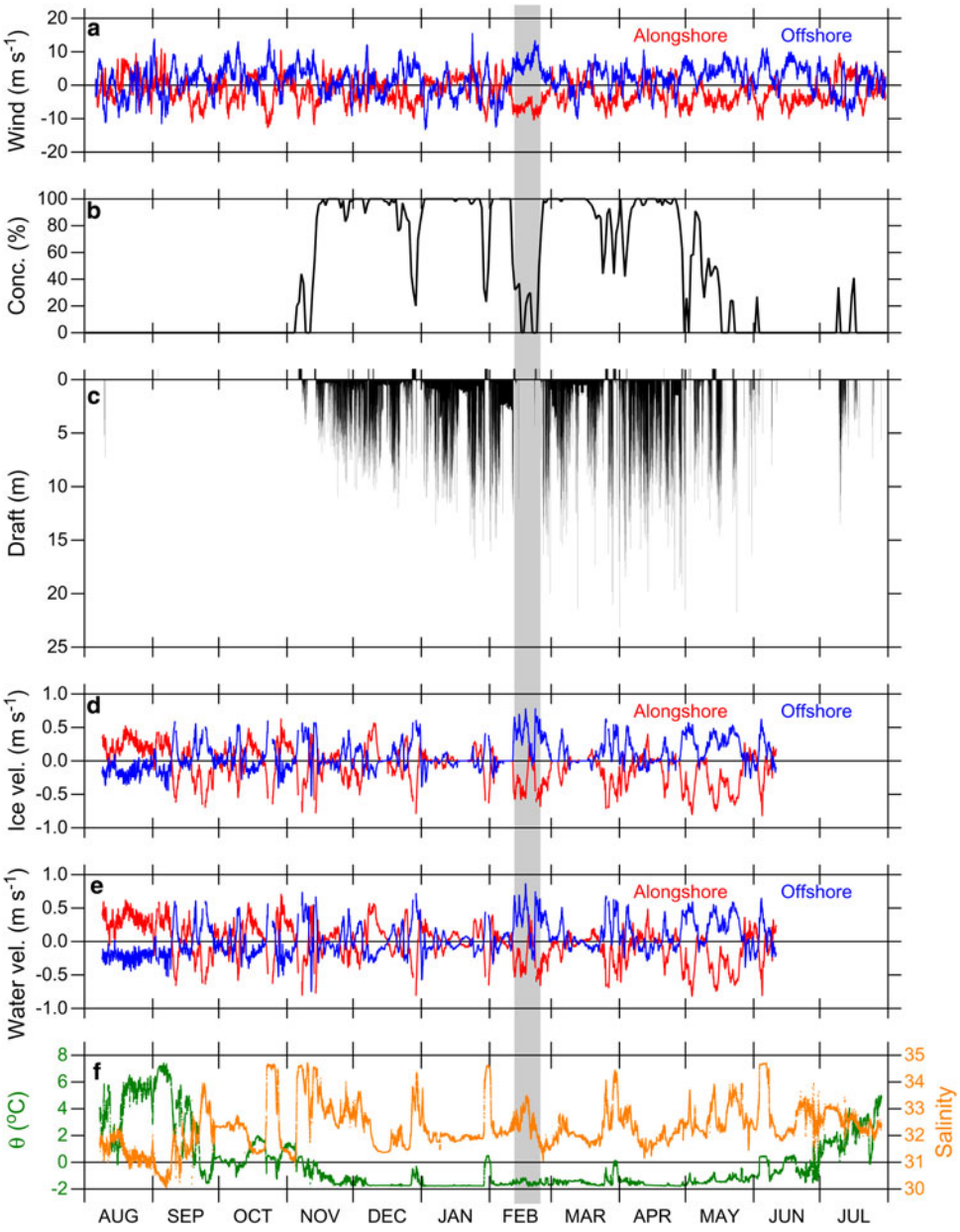

Fig. 2. Time series of (a) wind at the Barrow Wiley-Post Airport, (b) sea-ice concentration calculated by the Bootstrap Basic Algorithm (Comiso, 1995) at the AMSR-E grid point closest to the mooring, (c) sea-ice draft, (d) sea-ice velocity based on the ADCP bottom-track velocity and regressed velocity from the wind shown in (a) and the water velocity shown in (e), (e) water velocity in 18–20 m and (f) potential temperature and salinity at 41 m, from August 2009 to July 2010. In (a), (d) and (e), alongshore (29°T: °T indicating true bearing measured clockwise from the north) and offshore (299°T) components are shown. In (c), only data subsampled every minute are shown and missing or discarded values are indicated by −1 m. A prominent polynya period is denoted by shading.

respectively. From coincident IPS measurements of ice draft and airbone electromagnetic measurements of total ice-plus-snow thickness over the mooring location in 2010, Mahoney and others (2015) derived an average value of $\rho^* = 850 \pm 30$ kg m^{-3}. Assuming isostasy, we can express the relationship between total thickness, z_T, and ice draft, D, as:

$$z_T = z_i + z_s = \frac{\rho_w}{\rho^*} D = \alpha D \tag{2}$$

where ρ_w is the density of sea water, calculated to be 1025 kg m^{-3} from temperature and salinity measurements made at the mooring. Rearranging (1) allows us to determine the ratio between snow depth and ice thickness, β:

$$z_s = \beta z_i, \tag{3}$$

where

$$\beta = \frac{\rho^* - \rho_i}{\rho_s - \rho^*}. \tag{4}$$

Substituting (3) into (2) allows us to write an expression for the conversion factor from draft to ice thickness, γ:

$$z_i = \gamma D, \tag{5}$$

https://doi.org/10.1017/jog.2017.56 Published online by Cambridge University Press

where

$$\gamma = \frac{\alpha}{(1+\beta)}. \quad (6)$$

Assuming $\rho_i = 910 \pm 20$ kg m^{-3} (Timco and Frederking, 1996) and $\rho_s = 300 \pm 100$ kg m^{-3} (Warren and others, 1999), we derive estimates of $\beta = 0.11 \pm 0.07$ and $\gamma = 1.09 \pm 0.05$.

In addition to in situ data described above, we refer to the AMSR-E data at the closest grid point from the mooring location (black circle in Fig. 1). The presence of several AMSR-E grid points between the mooring and shore (gray circles) indicates that the data at the closest grid point (black circle) are free from land-contamination effects (Comiso and Parkinson, 2008).

In order to calculate heat loss from the ocean to the atmosphere, heat-budget calculations are carried out following Ohshima and others (2003). In the calculations, a balance among radiative, sensible and latent heat fluxes at the sea-ice surface and conductive flux through sea ice is considered and thermal inertia within sea ice is ignored. The value of latent heat of fusion for sea ice is mostly assumed to be a freshwater value of 0.334 MJ kg^{-1} based on Martin (1981) and following previous studies focusing on thin ice (Cavalieri and Martin, 1994; Signorini and Cavalieri, 2002; Tamura and Ohshima, 2011; Itoh and Others, 2012; Iwamoto and others, 2014 among others). For comparisons of results of heat-budget calculations and observed ice thicknesses, values of 0.293 and 0.249 MJ kg^{-1} corresponding to sea-ice salinities of 5 and 10, and temperature of −2°C are also used for thicker ice (>0.2 m) in the realistic cases with a snow cover. Note that heat flux from the ocean to the atmosphere is equivalent to sea-ice production under an assumption of ignored oceanic heat flux. The meteorological data used for these calculations are the ERA-Interim every 6 h at the closest grid point from the mooring location (open triangle in Fig. 1). Note that solar radiation is zero from mid-November till late January. These heat-budget calculations are performed to model thermodynamic growth from the initial condition of open water. These results are compared with time series of ice thickness obtained at the mooring and a mass-balance station (MBS; solid triangle in Fig. 1) which was deployed on level landfast sea ice near Utqiaġvik 43 km from the mooring location from 13 January to 14 June (Druckenmiller and others, 2009; Eicken and others, 2012; see http://seaice.alaska.edu/gi/data/barrow_massbalance for details of this observation). Also, these heat-budget calculations are performed based on measured ice thickness obtained from the IPS. These results are compared with those based on the estimated thin ice thickness from the AMSR-E data. Thin ice thickness is derived daily with a resolution of 6.25 km by an algorithm by Iwamoto and others (2013, 2014) based on comparisons between the polarization ratio of AMSR-E brightness temperatures from the 89 and 36 GHz channels and the thermal ice thickness. This thermal ice thickness is estimated from a heat-budget calculation using the ice-surface temperature from high-resolution (1.1 km resolution) clear-sky Moderate Resolution Imaging Spectroradiometer (MODIS) infrared data (Iwamoto and others, 2013, 2014). This algorithm detects thermal ice thickness ≤0.2 m. Estimated heat losses over thin ice (≤0.2 m) from the AMSR-E data are compared with those from the measured ice thickness to examine the validity of the AMSR-E derived product.

3. RESULTS AND DISCUSSION

3.1. Data overview and ice-drift conditions

At the mooring site, thick ice remaining from the 2008/09 growth season was observed in early August (Fig. 2c). New ice in the 2009/10 season was first observed in early November, after which the mooring site was mostly covered with sea ice until May. However, the time series of ice concentration and draft show several distinct events of low ice concentration and open water during the sea-ice season. In particular, there was a persistent open water event in mid-February (the period shaded in Fig. 2). During these events, the velocities of wind, ice and water had strong offshore components and warm, saline Atlantic Water with temperatures above the freezing point by >1°C and salinity >34 (Itoh and others, 2013) was present in December, January and March. Hirano and others (2016) have described the processes underlying these phenomena as follows. Strong offshore wind components generated a corresponding offshore flow of ice and water which formed a coastal polynya and caused subsequent upwelling of Atlantic Water from the intermediate layer. This upwelled warm Atlantic Water resulted in temporarily reduced sea-ice production in the polynya.

The cumulative drift (Fig. 3) shows dominant westward and west-southwestward ice movement with occasional northeastward and east-northeastward movement mainly in December and January (also see Fig. 2d). Note that the westward and west-southwestward movements have a significant offshore component (also see Fig. 5b below) leading to ice divergence and polynya formation. The northeastward and east-northeastward movements have an onshore component leading to ice convergence toward the coastline and ice deformation such as rafting and ridging.

3.2. Ice-draft statistical analysis

The probability-density distribution of the entire pseudo-spatial series of sea-ice draft (gray circles in Fig. 4a) reveals general characteristics of draft distribution in the region of observation. An exponential relationship (indicated by a black line in Fig. 4a) is obtained for this distribution in the

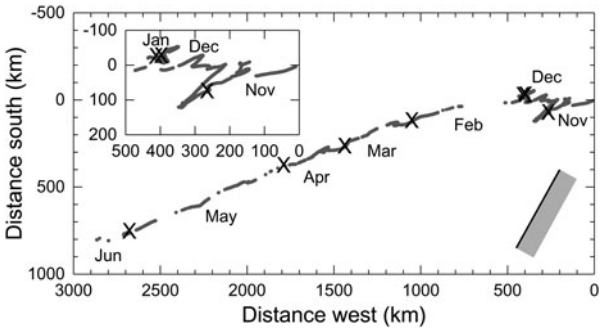

Fig. 3. Cumulative ice drift from 6 November 2009 to 9 June 2010 based on sea-ice velocity measured by an ADCP and a regression from the wind at Barrow Wiley-Post Airport and water velocity in 18–20 m measured by the same ADCP. Data with non-zero draft are plotted with gray dots and those with zero draft (open water) are not plotted. Crosses denote the first data of each month. The black line with the gray shaded region denotes the coastline orientation near the mooring. The inset is an enlarged figure of the first portion of the data.

https://doi.org/10.1017/jog.2017.56 Published online by Cambridge University Press

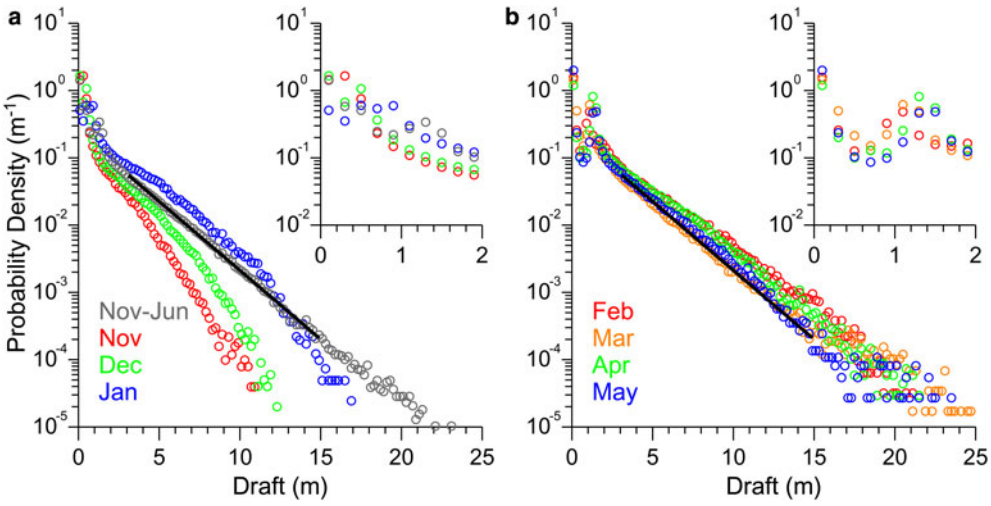

Fig. 4. Probability-density function of sea-ice draft. (a) Data during November–June (gray), November (red), December (green) and January (blue), and (b) February (red), March (orange), April (green) and May (blue). The bin size is 0.2 m. An exponential relationship obtained from the data during November–June in the draft range of 3–15 m is shown by a black line. For draft D, it is $f(D) = 0.237 \exp(-D/2.12)$. The insets are enlarged versions for the draft range ≤2 m.

range of 3–15 m, which represents the ridged and deformed component of the ice cover. Its e-folding scale of 2.12 m is close to 2.16 m in the coastal eastern Beaufort Sea during 1991/92 (Melling and Riedel, 1996) and smaller than 3.06 m during 1990 (Melling and Riedel, 1995), and larger than 1.50 m derived from the data obtained in the southern part of Davis Strait (61–65° N) (Wadhams and others, 1985). Thus, the relative abundance of thick ridged ice off Utqiaġvik can be close to that observed in the Beaufort Sea.

The distribution of ice draft over the entire measurement period exhibits two modes, with the primary corresponding drafts ≤0.2 m and the lesser, secondary corresponding to drafts in the range 1.2–1.4 m. Modal values in such distributions are taken to represent the draft of level, undeformed sea ice (Melling and Riedel, 1996; Behrendt and others, 2015). In this case, the primary mode indicates a persistent abundance of thin ice. Figure 4 also shows probability density functions of ice draft for each month from November to May indicating temporal evolution of draft. In November-January, the proportion of thick ice gradually increased (Fig. 4a). In February–May, the draft distribution did not change as much as in the previous months (Fig. 4b). The secondary mode mentioned above is assumed to represent the draft of thicker, older first-year sea ice, which will evolve over the course of the year (see inset panels in Fig. 4). We will examine seasonal variation of modal ice thicknesses in more detail later in Section 3.3.

Sea-ice statistics are summarized in Table 1. Monthly values clearly show sea-ice growth with increasing draft and concentration and decreasing level-ice fraction. The highest mean draft (1.82 m) and concentration (86.2%) and the lowest level-ice fraction (51.3%) observed in January are likely due to deformation such as ridging and rafting caused by onshore ice drift (Figs 2d, 3, 5b). The maximum

Table 1. Sea-ice statistics for the period from 6 November 2009 to 9 June 2010

	Ice path km	Draft m						Conc. %	Level ice	
		Mean	Std dev.	10%	90%	99%	Max.		Mean m	Fraction %
6 Nov–9 Jun	4565.7	1.27 (0.57)	1.76	0.06	3.40	8.35	25.25	44.5	0.52	64.0
Nov	504.7	0.62 (0.32)	0.92	0.05	1.59	4.59	10.98	51.8	0.30	75.1
Dec	670.9	0.83 (0.65)	1.24	0.06	2.34	6.06	12.44	78.0	0.33	71.3
Jan	239.3	1.82 (1.57)	2.02	0.20	4.70	9.18	16.91	86.2	0.64	51.3
Feb	763.0	1.70 (0.37)	2.22	0.05	4.52	10.28	21.01	21.7	0.61	56.0
Mar	500.2	1.33 (0.84)	1.77	0.07	3.30	8.46	25.25	63.3	0.62	66.5
Apr	547.6	1.80 (1.17)	2.06	0.06	4.41	9.73	21.52	64.9	0.85	59.3
May	1100.5	1.38 (0.25)	1.88	0.03	3.65	8.76	23.48	17.8	0.54	55.2

Also shown are monthly ice statistics from November to May. The ice path is the length of cumulative ice drift shown in Figure 3. For the draft statistics, areas of zero draft are excluded except for the mean drafts in parentheses. Values for 10, 90 and 99% indicate drafts that exceed these percentiles among all the drafts sorted in increasing order. Ice concentration is calculated from the spatial draft series. A section of the spatial draft series is classified as level ice if its draft varied by <±0.25 m over 10 m or longer after Wadhams and Horne (1980). Note that values of draft can be converted to those of thickness with a factor of ~1.09 based on the assumed densities of ice, snow and water.

https://doi.org/10.1017/jog.2017.56 Published online by Cambridge University Press

Table 2. Keel statistics for the period from 6 November to 9 June, and for each month from November to May

	Keel frequency km^{-1}				Mean of maximum keel draft m			
	$D > 9$ m	$D > 7$ m	$D > 5$ m	$D > 3$ m	$D > 9$ m	$D > 7$ m	$D > 5$ m	$D > 3$ m
6 Nov–9 Jun	0.48 (0.31)	1.17 (0.75)	2.75 (1.76)	6.28 (4.02)	11.17	9.22	7.29	5.37
Nov	0.03 (0.02)	0.19 (0.10)	0.90 (0.47)	3.80 (1.96)	10.13	8.19	6.27	4.39
Dec	0.16 (0.12)	0.63 (0.49)	2.15 (1.68)	6.10 (4.76)	10.10	8.39	6.58	4.80
Jan	1.10 (0.95)	2.85 (2.46)	6.08 (5.24)	12.52 (10.79)	10.85	9.02	7.37	5.58
Feb	1.33 (0.29)	2.86 (0.62)	5.97 (1.29)	11.45 (2.48)	11.55	9.60	7.67	5.84
Mar	0.63 (0.40)	1.53 (0.97)	3.58 (2.27)	8.01 (5.07)	11.65	9.45	7.41	5.46
Apr	1.20 (0.78)	2.70 (1.75)	5.81 (3.77)	12.02 (7.80)	11.25	9.38	7.51	5.64
May	1.17 (0.21)	2.71 (0.48)	6.30 (1.12)	14.54 (2.59)	11.00	9.21	7.31	5.35

Values are listed for keels deeper than 9, 7, 5 and 3 m. For the keel frequency, the values over ice and all the portions including open water (in parentheses) are shown. Mean values of maximum keel draft are calculated for keels exceeding 9, 7, 5 and 3 m.

draft of 25.25 m was observed in March. The highest monthly mean draft (1.82 m) as well as the overall mean draft is smaller than the mean draft of 2.01 m obtained in the coastal eastern Beaufort Sea during February–April in 1992–2003 (Melling and others, 2005). This comparison suggests generally thinner sea ice in the coastal Chukchi Sea than in a comparable region in the Beaufort Sea. Using a conversion factor from draft to thickness described earlier, the overall mean draft of 1.27 m can be converted to the mean thickness of 1.38 m. We will use the converted ice thickness data hereafter except for the keel statistics shown in Table 2.

Next, keel statistics are examined because they are important parameters to characterize each sea-ice region (Table 2). Keels are identified from the pseudo-spatial series of ice draft using a Rayleigh criterion (Wadhams and Davy, 1986) with a reference level of 0.50 m. This reference level is chosen close to the mean draft of level ice (0.52 m shown in Table 1). Keel frequency is defined as the average number of keels per km with a draft exceeding a given value. Most monthly keel frequencies were lower than those among the similar data obtained in the coastal eastern Beaufort Sea during April–May 1990 (1.58 and 4.42 km^{-1} for keels >9 and 5 m, respectively) and February–April 1992 (0.86 and 3.52 km^{-1} for keels >9 and 5 m, respectively) (Melling and Riedel, 1995, 1996). However, the monthly frequencies during the month of the highest mean draft (January) are

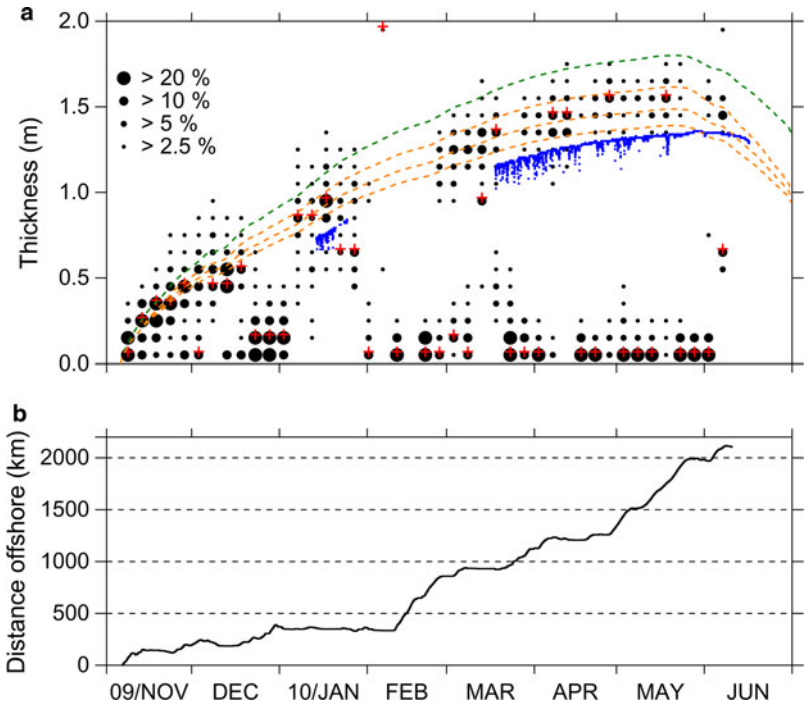

Fig. 5. (a) Evolution of ice-thickness distribution obtained by the IPS and its comparison with modeled thermodynamic growth and the MBS ice-thickness data (blue). The thickness distribution is evaluated every 5 days in 0.1 m bins. Symbol sizes denote their fractions as shown in the legends and red crosses indicate modes. The thermodynamic growth is calculated without snow (green) and with snow data (orange). The latent heat of fusion of sea ice is kept constant at 0.334 MJ kg^{-1} for green and lower orange curves, and is 0.334 MJ kg^{-1} for ice thickness ≤0.2 m, and 0.293 and 0.249 MJ kg^{-1} for thicker ice for middle and upper orange curves, respectively. (b) Offshore cumulative displacement of sea ice based on the measured and regressed ice velocities shown in Figure 2d.

https://doi.org/10.1017/jog.2017.56 Published online by Cambridge University Press

comparable with those values in the Beaufort Sea. From December to January, the mean draft increased significantly from 0.83 to 1.82 m and the level ice fraction dropped by 20% (Table 1). The highest monthly keel frequencies and these significant changes in January are likely associated with the onshore ice drift (Figs 2d, 3, 5b), resulting in convergence and in situ ridge building.

3.3. Thermodynamic ice growth

To examine the thermodynamic growth of sea ice during the study period, we calculated the modal draft (thickness) values at 5-day intervals (Fig. 5a), following a similar approach to those of Melling and Riedel (1996) and Behrendt and others (2015). Most 5-day ice thickness distributions exhibit two modal values. The larger of these modes increases monotonically over the season. The thinner mode mostly lies in the range ≤0.2 m and represents newly grown ice. In some cases, one of these modes is absent. Heat-budget calculations are performed to simulate sea-ice growth from the initial condition of open water on 6 November with and without snow (orange and green curves, respectively, in Fig. 5a) with a temporal resolution on the ERA-interim data of 6 h. In the case of snow-covered ice, we assumed a ratio of snow depth to ice thickness (β) of 0.11, based on the results of Mahoney and others (2015), as described in Section 2. Among these calculations, the value of latent heat of fusion of sea ice is set constant at 0.334 MJ kg^{-1} for the green and lower orange curves and it is set at 0.334 MJ kg^{-1} for thin ice ≤0.2 m, and decreased to 0.293 and 0.249 MJ kg^{-1} for thicker ice >0.2 m for the middle and upper orange curves, respectively. The start date of these calculations is rather arbitrary, but 6 November was chosen because it corresponds to the first observation of newly grown sea ice by the IPS. These calculation results are also compared with ice-thickness data obtained from the MBS. The calculated growth curves for a sea-ice cover with snow (orange) agree roughly with the growth observed at the MBS (blue), which suggests validity of the ice-growth model and assumed snow depth. The maximum calculated ice thickness with a constant value of latent heat of fusion and observed ice thickness are 1.39 and 1.36 m, respectively. The modal values corresponding to thicker first-year sea ice mostly lie between the two growth curves derived for ice with snow and decreased values of latent heat of fusion for thicker ice (the middle and upper orange curves). This result suggests that the evolution of ice corresponding to the larger modal values is driven mainly by thermodynamic ice growth. If the ice observed here was mostly produced locally (and assuming the snow cover estimate is accurate), this result also suggests that decreased values of latent heat of fusion are more adequate. If the constant larger value of latent heat of fusion was more adequate, however, the fact that the modal values of thicker ice at the mooring site mostly exceed the derived estimates for ice covered with snow may suggest that the mooring sampled ice advected from the Northeast. Such ice may both have been subjected to colder weather and lower

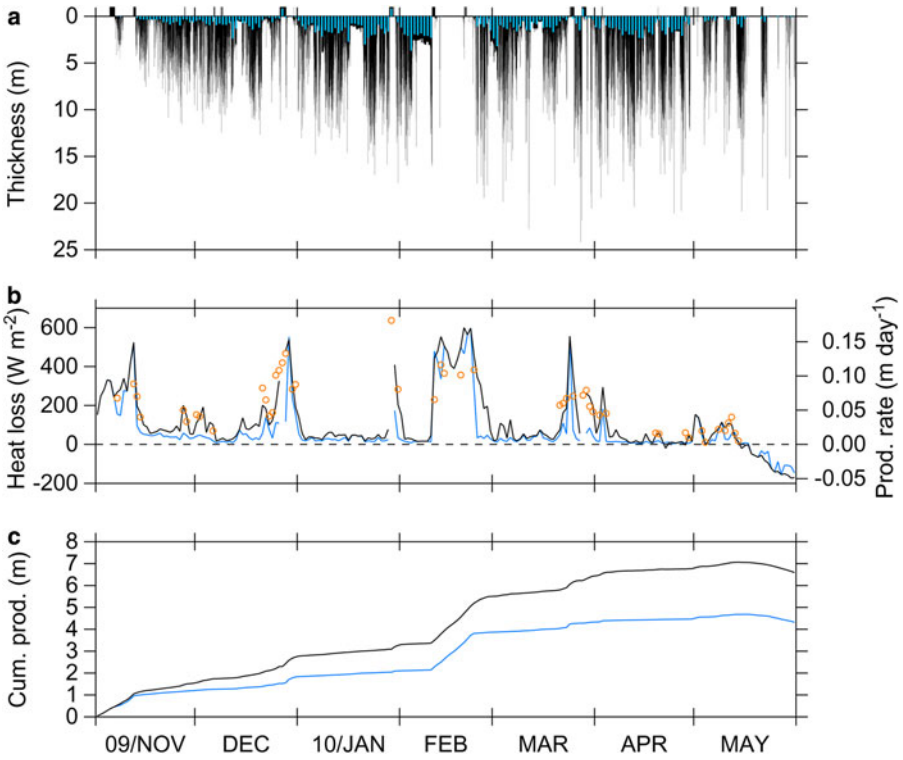

Fig. 6. Time series of (a) ice thickness converted from ice draft measured every second by the IPS (black) and its daily average (blue), and (b) heat losses calculated by heat-budget calculations based on the measured ice thickness (black) and its daily average (blue) along with heat loss based on the thicknesses estimated from the AMSR-E data (orange). (c) shows cumulative ice production based on the measured ice thickness (black) and its daily average (blue). Note that the heat losses in (b) are also expressed in terms of sea-ice production (*y*-axis on the right) since oceanic heat flux is not considered in the heat-budget calculation here. Effects of snow are not included in the heat-budget calculations.

https://doi.org/10.1017/jog.2017.56 Published online by Cambridge University Press

snow accumulation, potentially explaining the discrepancy in thickness. These results along with the observed maximum modal value in the 1.5–1.6 m bin suggest that sea ice can grow thermodynamically to ~1.5 m in the observed and upstream regions. Note that these observed modal values are comparable with the ones observed by Melling and Riedel (1996) further east in the coastal Beaufort Sea. Low-draft modal values occurred during the periods of offshore ice movement (Fig. 5b) indicating ice divergence associated with coastal polynya formation in the region. The latter modal values in the thickness bin ≤0.2 m were dominant in February and May when offshore displacement was large and new ice started growing in the opening coastal polynya.

3.4. Heat-loss calculations

3.4.1. Importance of subgrid-scale processes in the ice-thickness assessments

A disproportionately large fraction of the heat loss from ocean to atmosphere and the resulting sea-ice formation occur in regions of open water and thin ice. The magnitude of the area-integrated heat loss is therefore sensitive to the way in which ice thickness is evaluated in a given area if ice thickness is non-uniformly distributed. Using the combination of freeboard data from Ice, Cloud and Land Elevation Satellite (ICESat), snow-depth data from AMSR-E over first-year ice and climatological data over multiyear ice, Kurtz and others (2009) mapped ice and snow thickness over the entire Arctic with the ~70 m spatial resolution of ICESat. Using these high-resolution thickness maps, they calculated an Arctic-wide heat loss through sea ice and snow in fall and winter that was about one-third higher than that based on their down-sampled 25 km average. This difference is attributed to the nonlinear dependence of heat loss on ice thickness. Komuro and Suzuki (2013) calculated surface heat loss in the Arctic with subgrid-scale ice-thickness distribution in 15 categories (from 0.1–0.2 to >14.0 m) using an ice/ocean coupled model. (Their model's zonal resolution is 1.4°, whereas meridional resolution varies from 0.5° in the equatorial and polar regions to 1.4° in the mid-latitude region.) Komuro and Suzuki's modeling study showed results consistent with those by Kurtz and others (2009) and suggested a factor (0.525 for the Arctic) to be applied to modeled sea-ice thickness if the subgrid-scale ice-thickness distribution is not considered in order to compensate for the lack of thickness distribution within each grid in their model.

Here, we examine effects of non-uniformity of ice thickness on heat loss calculated based on our IPS data measured every second. Note that this dataset is in sub-meter spatial scales and much finer than that used by Kurtz and others (2009). Obviously, heat loss (equivalent to ice production neglecting oceanic heat flux) was intense during polynya periods with open water and/or thin ice (Figs 6a, b). Heat losses shown in Figure 6b are daily-averaged values from values calculated every second using interpolated ERA-interim data with observed 1 s IPS ice thickness data (black) and their daily-averaged values (blue). In general, the calculated values of heat loss based on the 1 s IPS thickness data are larger than those based on the daily averages. Cumulative ice growth values based on 1 s and daily-averaged IPS data reached maxima of 7.06 and 4.69 m, respectively (Fig. 6c). The average value of daily cumulative sea-ice drift is 20.8 km (with its standard deviation of 19.2 km). We consider this value as a spatial scale corresponding to the daily average. Namely, considering daily-averaged sea-ice thickness is equivalent to smooth spatial non-uniformity of sea ice over this spatial scale. The two estimates were quite different when thick ice was observed at the edge of a polynya and they were similar when a polynya was observed for longer than a day. Clearly, these periods correspond to those of high and low spatial non-uniformity of ice thickness.

Taking advantage of high temporal resolution, the measured ice-thickness time series are averaged over various timescales from 10 min to 10 days in addition to 1 day and heat-budget calculations are repeated based on these average values. These calculations are performed with and without snow. As the result shown in Figure 5, snow depth is assumed to be 11% of ice thickness. Figure 7 clearly shows that the heat loss derived from time series data averaged over different intervals decreases with an increase in the temporal scale, and hence also spatial scale based on ice velocity. This tendency is more significant if snow over ice is considered (open circle). Especially, the decrease in heat loss is fastest over temporal scales shorter than a day. With the averaged sea-ice thickness over 1- and 5-day

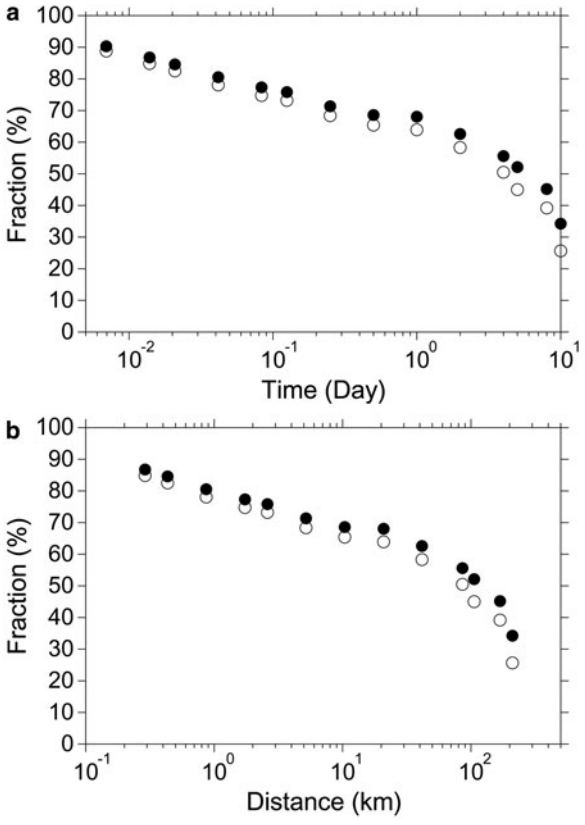

Fig. 7. (a) Normalized heat losses (corresponding to ice production) based on measured IPS ice thickness averaged over various timescales from 10 min to 10 days to that based on measured IPS thickness at every second. Heat-budget calculations are performed over 200 days from 1 November to 19 May. Open and solid circles represent calculations with and without snow cover, respectively. (b) Similar to (a) except the fractions are plotted against the distance scales corresponding to the various time scales. Note the logarithmic scale of the *x*-axes.

https://doi.org/10.1017/jog.2017.56 Published online by Cambridge University Press

periods, which correspond to spatial scales of ~20 and 100 km, the resultant heat losses without snow are about two-thirds and a half of that with the raw ice thickness every second, respectively. These results indicate that it is crucial to consider the non-uniformity of ice thickness to accurately derive heat loss (correspondng to sea-ice production) in coarse-resolution models without subgrid-scale ice-thickness distribution and results from such coarse-resolution models should be treated with caution and modified (Komuro and Suzuki, 2013).

3.4.2. Comparison with AMSR-E thin ice data

Due to their oceanographic importance for maintaining the Arctic halocline layer, heat loss and sea-ice production in polynyas have been estimated by many remote-sensing studies in the region of observation (e.g., Cavalieri and Martin, 1994; Martin and others, 2004, 2005; Tamura and Ohshima, 2011; Itoh and others, 2012; Iwamoto and others, 2013, 2014). However, these estimates have not been validated by in situ data. Here, we compare the measured and satellite-derived ice thicknesses in terms of the calculated heat loss (corresponding to ice production) as shown in Figure 6b. Figure 8 clearly shows that heat loss based on the AMSR-E derived daily ice thickness is better correlated with that based on the IPS thickness measured every second. The bias and RMS difference between heat losses from AMSR-E and 1 s IPS data are -3.5 W m^{-2} (-0.001 m day^{-1}) and 78 W m^{-2} (0.02 m day^{-1}), respectively (Fig. 8a). These values are much smaller than those derived from AMSR-E and daily averaged IPS data of 84 W m^{-2} (0.02 m day^{-1}) and 141 W m^{-2} (0.04 m day^{-1}) (Fig. 8b). The bias is defined by subtracting the result based on the IPS data from that based on the AMSR-E data. This result suggests the validity of the AMSR-E derived thin ice thickness and resulting heat loss shown in Iwamoto and others (2013, 2014). Note that the AMSR-E thin ice thickness is the thermal thickness determined from matching the polarization ratio of AMSR-E brightness temperatures and the thermal ice thickness estimated from a heat-budget calculation using the ice surface temperature from MODIS infrared data (Iwamoto and others, 2013, 2014). Thus, it is derived from the averaged surface temperature of ice with a variety of thicknesses, not from the averaged ice thickness in each grid cell. As a result, the non-uniformity of ice thickness is considered in this method and the resulting daily heat loss (ice production) agrees better with that derived from the IPS thickness every second (Fig. 8a).

4. SUMMARY

In this study, we reveal detailed characteristics of sea-ice draft (thickness) in the coastal northeastern Chukchi Sea (Fig. 1), obtained from time series data collected for the first time in the region by a moored ice-profiling sonar in 2009/10. Time series data show seasonal increase in sea-ice draft, which is occasionally interrupted by the appearances of coastal polynya and upwelled Atlantic Water caused by offshore winds (Fig. 2). The sea-ice draft distribution for the period from early November to early June (Fig. 4a) indicates the abundance of ice that is comparable with or thinner than in the coastal eastern Beaufort Sea. The rapid increase in the fraction of thicker ice from December to January (Fig. 4a and Table 1) corresponded to the minimal drift in January (Fig. 3) and the resulting rapid decrease of the level-ice fraction (Table 1). The mean sea-ice draft and its converted thickness from early November to early June are 1.27 and 1.38 m, respectively. Keel statistics (Table 2) show frequencies of large keels are lower than those in the coastal eastern Beaufort Sea. Distributions of sea-ice thickness every 5 days clearly reveal two modes: a thinner mode ≤0.2 m and a larger mode growing seasonally up to ~1.5 m (Fig. 5a). The larger mode is considered to be thermodynamically grown first-year ice, and its thickness is larger than or similar to the results of heat-budget calculations with re-analysis meteorological and snow-depth data derived from

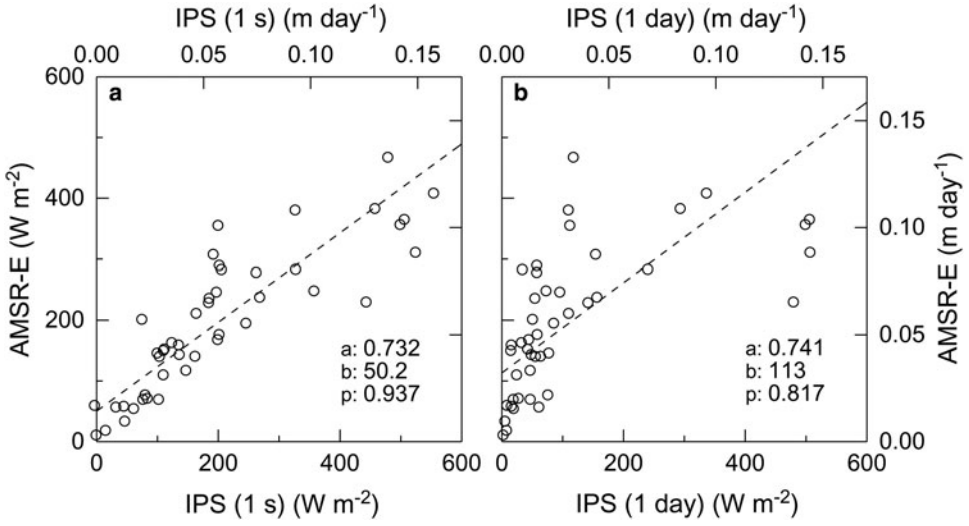

Fig. 8. Scatter diagrams of daily heat loss calculated by heat-budget calculations based on ice thickness measured by the IPS and estimated from AMSR-E. Values are also expressed in terms of ice-production rate per day with an assumption of no oceanic heat flux. The heat losses calculated with the IPS thickness every second and its daily average are shown in (a) and (b), respectively. Dashed lines are obtained by principal component analyses. Values *a* and *b* are the slope and *y*-intercept, and *p* is the proportion of the variance explained by the principal component.

https://doi.org/10.1017/jog.2017.56 Published online by Cambridge University Press

observations at the mooring site (orange curves in Fig. 5a) depending on the value of latent heat of fusion. This fact may indicate that the mooring sampled sea ice of greater thickness due to more severe weather conditions and potentially less snow accumulation upstream in the Beaufort Sea as well as locally produced ice. However, further work is needed to identify its origins.

Due to nonlinear dependence of heat loss (and ice production) on sea-ice thickness, it is crucial to capture the non-uniformity of sea-ice thickness over time (and space) accurately in observational data and modeling results to minimize errors in estimates of heat loss. A comparison of heat losses calculated with observed sea-ice thickness averaged over various timescales, corresponding to various spatial scales, clearly illustrates this fact (Figs 6b, c, 7). Based on the observational data used in this study, heat loss with an assumption of no snow cover is reduced to about two thirds and a half of the value estimated with the original 1 s interval data if ice-thickness data are averaged over 1 day and 5 days, respectively (Fig. 7a). These timescales roughly correspond to spatial scales of 20 and 100 km (Fig. 7b), which are typical resolutions of large-scale numerical models. Furthermore, the reduction is enhanced with snow cover. The heat-loss estimate based on the AMSR-E data is compared with those based on the observed ice-thickness data (Fig. 8). It corresponds well with the estimate based on the 1 s measured data (Fig. 8a), which indicates the validity of a thin ice thickness algorithm and the resulting heat-loss estimate based on the AMSR-E data in Iwamoto and others (2013, 2014).

This study reveals detailed characteristics of sea-ice thickness in the Chukchi Sea for the first time. However, findings in this study are based on data from a single mooring deployed in 2009/10. Thus, it is important to analyze other existing data and acquire new data in the Chukchi Sea to examine temporal and spatial variability of sea-ice thickness. Such data will be valuable additions to enhance our understanding of recent decline of sea-ice extent in the Pacific Arctic.

ACKNOWLEDGEMENTS

We thank the staff of CH2M HILL Polar Services, the Barrow Arctic Science Consortium and UMIAQ for field support in Utqiaġvik. We are also grateful to the North Slope Borough Department of Wildlife Management for use of their boat and assistance from their staff. Comments from two anonymous reviewers were very helpful. AMSR-E data were provided by the US National Snow and Ice Data Center. In Japan, support was provided by Grants in Aid for Scientific Research (awards 20221001, 23654163 and 15H03721), the Green Network of Excellence (GRENE) Arctic Climate Change Research Project and Arctic Research for Sustainability (ArCS) Project from the Japanese Ministry of Education, Culture, Sports, Science and Technology (MEXT), a research fund for Global Change Observation Mission 1st-Water of the Japan Aerospace Exploration Agency (JAXA) and Global Station for Arctic Research, a project of Global Institution for Collaborative Research and Education at Hokkaido University. In the USA, support was provided by the US National Science Foundation Seasonal Ice Observing Network award OPP-0856867 and the US Department of Homeland Security Center for Island, Maritime and Extreme Environment Security (CIMES).

REFERENCES

ASL Environmental Sciences (2014) *IPS processing toolbox™ user's guide*. Sidney

Behrendt A, Dierking W, Fahrbach E and Witte H (2013) Sea ice draft in the Weddell Sea, measured by upward looking sonars. *Earth Syst. Sci. Data*, **5**, 209–226 (doi: 10.5194/essd-5-209-2013)

Behrendt A, Dierking W and Witte H (2015) Thermodynamic sea ice growth in the central Weddell Sea, observed in upward-looking sonar data. *J. Geophys. Res.*, **120**, 2270–2286 (doi: 10.1002/2014JC010408)

Cavalieri DJ and Martin S (1994) The contribution of Alaskan, Siberian, and Canadian coastal polynyas to the cold halocline layer of the Arctic Ocean. *J. Geophys. Res.*, **99**(C9), 18343–18362

Comiso J (1995) SSM/I ice concentrations using the Bootstrap algorithm. *Natl. Aeronaut. Space Admin. Ref. Pub.*, **1350**, 50

Comiso JC and Parkinson CL (2008) Arctic sea ice parameters from AMSR-E data using two techniques and comparisons with sea ice from SSM/I. *J. Geophys. Res.*, **113**, C02S05 (doi: 10.1029/2007JC004255)

Druckenmiller ML, Eicken H, Johnson MA, Pringle DJ and Williams CC (2009) Towards an integrated coastal sea-ice observatory: system components and a case study at Barrow, Alaska. *Cold Reg. Sci. Technol.*, **56**(2–3), 61–72 (doi: 10.1016/j.coldregions.2008.12.003)

Eicken H and 5 others (2009, updated in 2012). Automated ice mass balance site (SIZONET). UCAR/NCAR – CISL – ACADIS. http://dx.doi.org/10.5065/D6MW2F2H

Fukamachi Y and 5 others (2003) Variability of sea-ice draft off Hokkaido in the Sea of Okhotsk revealed by a moored ice-profiling sonar in winter of 1999. *Geophys. Res. Lett.*, **30**(7), 1376 (doi: 10.1029/2002GL016197)

Fukamachi Y and 5 others (2006) Sea-ice thickness in the southwestern Sea of Okhotsk revealed by a moored ice-profiling sonar. *J. Geophys. Res.*, **111**, C09018 (doi: 10.1029/2005JC003327)

Fukamachi Y and 8 others (2009) Direct observations of sea-ice thickness and brine rejection off Sakhalin in the Sea of Okhotsk. *Conti. Shelf Res.*, **29**, 1541–1548 (doi: 10.1016/j.csr.2009.04.005)

Hirano D and 8 others (2016) A wind-driven, hybrid latent and sensible heat coastal polynya off Barrow, Alaska. *J. Geophys. Res.*, **121**, 980–997 (doi: 10.1002/2015JC011318)

Itoh M and 5 others (2012) Interannual variability of Pacific Winter Water inflow through Barrow Canyon from 2000 to 2006. *J. Oceanogr.*, **68**(4), 575–592 (doi: 10.1007/s10872-012-0120-1)

Itoh M, Nishino S, Kawaguchi Y and Kikuchi T (2013) Barrow Canyon volume, heat, and freshwater fluxes revealed by long-term mooring observations between 2000 and 2008. *J. Geophys. Res.*, **118**, 1–17 (doi: 10.1002/jgrc.20290)

Iwamoto K, Ohshima KI, Tamura T and Nihashi S (2013) Estimation of thin ice thickness from AMSR-E data in the Chukchi Sea. *Int. J. Remote Sens.*, **34**(2), 468–489 (doi: 10.1080/01431161.2012.712229)

Iwamoto K, Ohshima KI and Tamura T (2014) Improved mapping of sea ice production in the Arctic Ocean using AMSR-E thin ice thickness algorithm. *J. Geophys. Res.*, **119**, 3574–3594 (doi: 10.1002/2013JC009749)

Komuro Y and Suzuki T (2013) Impact of subgrid-scale ice thickness distribution on heat flux on and through sea ice. *Ocean Modell.*, **71**, 13–25 (doi: 10.1016/j.ocemod.2012.08.004)

Krishfield RA and 6 others (2014) Deterioration of perennial sea ice in the Beaufort Gyre from 2003 to 2012 and its impact on the

https://doi.org/10.1017/jog.2017.56 Published online by Cambridge University Press

oceanic freshwater cycle. *J. Geophys. Res.*, **119**, 1217–1305 (doi: 10.1002/2013JC008999)
Kurtz NT and 6 others (2009) Estimation of sea ice thickness distributions through the combination of snow depth and satellite laser altimetry data. *J. Geophys. Res.*, **114**(C10), C10007 (doi: 10.1029/2009JC005292)
Ladd C, Mordy CW, Salo SA and Stabeno PJ (2016) Winter water properties and the Chukchi Polynya. *J. Geophys. Res.*, **121**, 5516–5534 (doi: 10.1002/2016JC011918)
Mahoney AR, Eicken H and Shapiro L (2007) How fast is landfast sea ice? A study of the attachment and detachment of nearshore ice at Barrow, Alaska. *Cold Reg. Sci. Technol.*, **47**(3), 233–255 (doi: 10.1016/j.coldregions.2006.09.005)
Mahoney AR, Eicken H, Gaylord AG and Gens R (2014) Landfast sea ice extent in the Chukchi and Beaufort Seas: the annual cycle and decadal variability. *Cold Reg. Sci. Technol.*, **103**, 41–56 (doi: 10.1016/j.coldregions.2014.13.003)
Mahoney AR and 8 others (2015) Taking a look at both sides of the ice: comparison of ice thickness and drift speed as observed from moored, airborne and shore-based instruments near Barrow, Alaska. *Ann. Glaciol.*, **56**(69), 363–372 (doi: 10.3189/2015AoG69A565)
Martin S (1981) Frazil ice in rivers and oceans. *Annu. Rev. Fluid Mech.*, **13**, 379–397 (doi: 10.1146/annurev.fl.13.010181.002115)
Martin S, Drucker R, Kwok R and Holt B (2004) Estimation of the thin ice thickness and heat flux for the Chukchi Sea Alaskan coast polynya from Special Sensor Microwave/Imager data. *J. Geophys. Res.*, **109**, C10012 (doi: 10.1029/2004JC002428)
Martin S, Drucker R, Kwok R and Holt B (2005) Improvements in the estimates of ice thickness and production in the Chukchi Sea polynyas derived from AMSR-E. *Geophys. Res. Lett.*, **32**, L05505 (doi: 10.1029/2004GL022013)
Melling H and Lewis EL (1982) Shelf drainage flows in the Beaufort Sea and their effect on the Arctic Ocean pycnocline. *Deep-Sea Res.*, **29**(8A), 967–985
Melling H and Riedel DA (1995) The underside topography of sea ice over the continental shelf of the Beaufort Sea in the winter of 1990. *J. Geophys. Res.*, **100**(C7), 13641–13653
Melling H and Riedel DA (1996) Development of seasonal pack ice in the Beaufort Sea during the winter of 1991–1992: a view from below. *J. Geophys. Res.*, **101**(C5), 11975–11991
Melling H, Johnston PH and Riedel DA (1995) Measurements of the underside topography of sea ice by moored subsea sonar. *J. Atmos. Oceanic Technol.*, **12**(3), 589–602
Melling H, Riedel DA and Gedalof Z (2005) Trends in the draft and extent of seasonal pack ice, Canadian Beaufort Sea. *Geophys. Res. Lett.*, **32**, L24501 (doi: 10.1029/2005GL024483)
Ohshima KI, Watanabe T and Nihashi S (2003) Surface Heat Budget of the Sea of Okhotsk during 1987-2001 and the Role of Sea Ice on it. *J. Meteorol. Society Jpn.*, **81**(4), 653–667
Paquette RG and Bourke R (1974) Observation on the coastal current of Arctic Alaska. *J. Mar. Res.*, **32**, 195–207
Signorini SR and Cavalieri DJ (2002) Modeling dense water production and salt transport from Alaskan coastal polynyas. *J. Geophys. Res.*, **107**(C9), 3051 (doi: 10.1029/2000JC000491)
Singh RK, Oza SR, Vyas NK and Sarkar A (2011) Estimation of thin ice thickness from the advanced microwave scanning radiometer-EOS for Coastal Polynyas in the Chukchi and Beaufort Seas. *IEEE Trans. Geosci. Remote Sens.*, **49**, 2293–2298 (doi: 10.1109/TGRS.2011.2123101)
Strass VH (1998) Measuring sea ice draft and coverage with moored upward looking sonars. *Deep-Sea Res. I*, **45**(4–5), 795–818
Tamura T and Ohshima KI (2011) Mapping of sea ice production in the Arctic coastal polynyas. *J. Geophys. Res.*, **116**, C07030 (doi: 10.1029/2010JC0068586)
Timco GW and Frederking RMW (1996) A review of sea ice density. *Cold Reg. Sci. Technol.*, **24**(1), 1–6 (doi: 10.1016/0165-232X(95)00007-X)
Valenti VA (2015) *Sea ice parameters for actions on offshore structures in the Beaufort and Chukchi Seas*. University of Alaska Anchorage, Anchorage
Wadhams P and Davy RJ (1986) On the spacing and draft distributions for pressure ridge keels. *J. Geophys. Res.*, **91**(C9), 10697–10708
Wadhams P and Horne RJ (1980) An analysis of ice profiles obtained by submarine sonar in the Beaufort Sea. *J. Glaciol.*, **25**(93), 401–424
Wadhams P, McLaren AS and Weintraub R (1985) Ice thickness distribution in Davis Strait in February from submarine sonar profiles. *J. Geophys. Res.*, **90**(C1), 1069–1077
Warren SG and 6 others (1999) Snow depth on Arctic sea ice. *J. Climate*, **12**(6), 1814–1829 (doi: 10.1175/1520-0442(1999)012<1814:SDOASI>2.0.CO;2)
Weingartner TJ, Cavalieri DJ, Aagaard K and Sasaki Y (1998) Circulation, dense water formation, and outflow on the northeast Chukchi shelf. *J. Geophys. Res.*, **103**(C4), 7647–7661
Winsor P and Björk G (2000) Polynya activity in the Arctic Ocean from 1958 to 1997. *J. Geophys. Res.*, **105**(C4), 8789–8803
Winsor P and Chapman DC (2002) Distribution and interannual variability of dense water production from coastal polynyas on the Chukchi Shelf. *J. Geophys. Res.*, **107**(C7), 3079 (doi: 10.1029/2001JC000984)

MS received 24 March 2017 and accepted in revised form 18 August 2017

https://doi.org/10.1017/jog.2017.56 Published online by Cambridge University Press